nature physics

Article

https://doi.org/10.1038/s41567-023-02008-4

Layer-by-layer disentanglement of Bloch states

Received: 16 June 2022

Accepted: 27 February 2023

Published online: 23 March 2023

Check for updates

Woojoo Lee[1,6], **Sebastian Fernandez-Mulligan**[1,5,6], **Hengxin Tan**[2], **Chenhui Yan**[1], **Yingdong Guan**[3], **Seng Huat Lee**[3,4], **Ruobing Mei**[3], **Chaoxing Liu**[3], **Binghai Yan**[2], **Zhiqiang Mao**[3] & **Shuolong Yang**[1]

Layer-by-layer material engineering has produced interesting quantum phenomena such as interfacial superconductivity and the quantum anomalous Hall effect. However, probing electronic states layer by layer remains challenging. This is exemplified by the difficulty in understanding the layer origins of topological electronic states in magnetic topological insulators. Here we report a layer-encoded frequency-domain photoemission experiment on the magnetic topological insulator $(MnBi_2Te_4)(Bi_2Te_3)$ that characterizes the origins of its electronic states. Infrared laser excitations launch coherent lattice vibrations with the layer index encoded by the vibration frequency. Photoemission spectroscopy then tracks the electron dynamics, where the layer information is carried in the frequency domain. This layer–frequency correspondence shows wavefunction relocation of the topological surface state from the top magnetic layer into the buried second layer, reconciling the controversy over the vanishing broken-symmetry energy gap in $(MnBi_2Te_4)(Bi_2Te_3)$ and its related compounds. The layer–frequency correspondence can be harnessed to disentangle electronic states layer by layer in a broad class of van der Waals superlattices.

Manipulating electronic, magnetic and lattice degrees of freedom layer by layer allows us to engineer materials' electronic properties at the level of single atomic sheets. This principle is manifested in the fabrication of magnetic topological insulators, whereby magnetism breaks the time-reversal symmetry and enables exotic topological phases of matter such as the axion insulators[1] and quantum anomalous Hall insulators[2]. Notably, the realization of these topological quantum phases relies on the fact that specific electronic states reside on the magnetic layers. A surgical probe of electronic states with both a meV energy resolution and a layer-wise spatial resolution is key to unveiling the topological characters of interlaced quantum materials.

We focus on one of the most promising material candidates for realizing high-temperature topological orders: $(MnBi_2Te_4)(Bi_2Te_3)_n$ superlattices[3]. These superlattices consist of magnetic $MnBi_2Te_4$ (MBT) layers interleaved with non-magnetic Bi_2Te_3 (BT) layers. Varying the stacking order leads to a multitude of topological phases[1,2]. However, notable controversies have arisen over the coupling between the topological surface state (TSS) and the broken-symmetry MBT layers[3–12]. Angle-resolved photoemission spectroscopy (ARPES)[6] and scanning tunnelling spectroscopy (STS)[13] studies have led to the theoretical proposal that the TSS can be decoupled from the top MBT layer. However, owing to the lack of a direct layer resolution, the picture of TSS relocation remains contentious. This is reflected from the alternative interpretation of the STS results[13] using Rashba-split electronic states[11], underscoring the pressing need to develop spectroscopic techniques with layer resolution to show the layer origins of the TSS and other key electronic states.

---

[1]Pritzker School of Molecular Engineering, The University of Chicago, Chicago, IL, USA. [2]Department of Condensed Matter Physics, Weizmann Institute of Science, Rehovot, Israel. [3]Department of Physics, Pennsylvania State University, University Park, PA, USA. [4]2D Crystal Consortium, Materials Research Institute, Pennsylvania State University, University Park, PA, USA. [5]Present address: Department of History, Yale University, New Haven, CT, USA. [6]These authors contributed equally: Woojoo Lee, Sebastian Fernandez-Mulligan. ✉e-mail: yangsl@uchicago.edu

https://doi.org/10.1038/s41567-023-02008-4

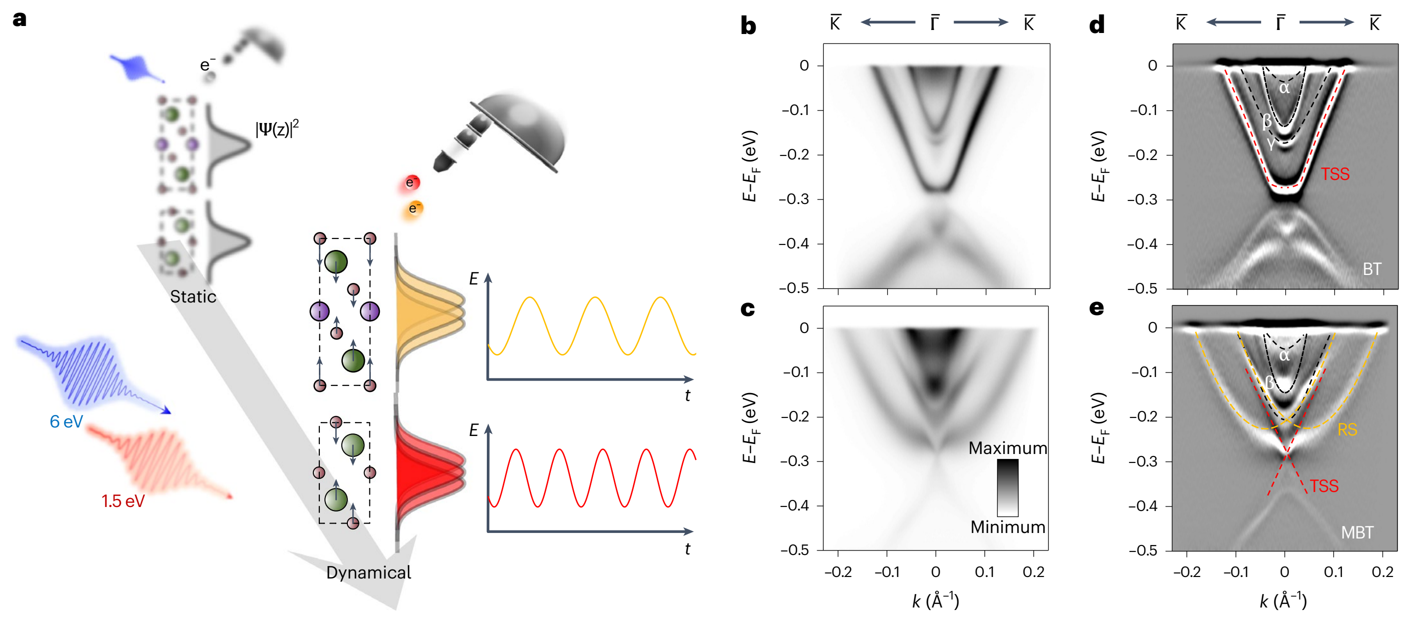

Fig. 1 | Experimental scheme and the electronic band structure of an (MBT)(BT) superlattice. a, Schematics of ARPES and trARPES measurements. **b**,**c**, Static μ-ARPES spectra cutting through $\bar{\Gamma}-\bar{K}$ on the BT termination (**b**) and the MBT termination (**c**). **d**,**e**, Second derivative images of the spectra on the BT termination (**d**) and the MBT termination (**e**). The black, red and yellow dashed lines highlight the bulk bands, TSSs and RS, respectively.

Here we demonstrate a layer-encoded frequency-domain (FD) ARPES experiment to disentangle electronic states layer by layer in (MBT)(BT) superlattices. Infrared pump pulses launch coherent phonon modulations, serving as the intrinsic tuning knob to probe electron–phonon coupling[14–16]. The crystal structure of our targeted material, (MBT)(BT), differs layer by layer, yielding layer-specific coherent phonon frequencies. Subsequently, the induced energy oscillations of the electronic states are measured by time-resolved ARPES (trARPES) and linked to different layers through the decomposition in the frequency domain. This layer–frequency correspondence shows a surprising wavefunction relocation of the TSS into the buried non-magnetic layers, and provides a critical hint to resolve the outstanding mystery of the near-gapless TSS. Our work is one of the first milestones in ultrafast spectroscopy connecting the spatial and frequency domains, conceptualized as 'seeing by listening'.

We performed static micro (μ)-ARPES measurements[17] to characterize the occupied electronic band structures on the two terminations of (MBT)(BT) (Fig. 1b–e). On the BT termination, three parabolic bands near $\bar{\Gamma}$ were observed and labelled as α, β and γ. On the MBT termination, only the α and β bands were identified. We characterized the α, β and γ bands as bulk conduction bands on the basis of the comparison with density functional theory (DFT) (Supplementary Fig. 1) and previous ARPES studies[10]. In addition, we observed the TSS on the BT termination, which hybridized with a bulk valence band (Fig. 1b,d). The Dirac point is observed near −0.37 eV. On the MBT termination, we observed a distinct electron-like pocket with a Fermi momentum of 0.19 Å^{-1} (Fig. 1c,e). Circular dichroism ARPES measurements on a series of (MBT)$(\text{BT})_n$ compounds suggest that this feature probably originates from a pair of Rashba-split pockets with a coupling constant $\alpha_R \sim 0.7$ eV Å (Supplementary Note 1). Therefore, we denote this pair of bands as Rashba-split states (RS). A V-shaped feature on the MBT termination with a binding energy of −0.2 eV originates from the TSS–RS hybridization (Supplementary Note 1).

We show the ultrafast electron dynamics on the BT termination by trARPES (Fig. 2). All investigations were performed consistently on the targeted sample position after ensuring a precise beam alignment between static ARPES and trARPES set-ups (Supplementary Note 2). To account for model-dependent systematic uncertainties, we fitted time-dependent energy distribution curves (EDCs) to various models involving single or multiple Lorentzian peaks (Supplementary Note 3), and extracted the consistent binding energy dynamics of the TSS (Fig. 2b). Fast Fourier transforms (FFTs) of the coherent energy oscillations ($\delta E(t)$) exhibit a dominant 1.8-THz mode along with two subdominant modes at 1.2 THz and 3.4 THz (Supplementary Fig. 8). Comparison with Raman spectroscopy allows us to identify the 1.2-THz and 1.8-THz modes as the c-axis A_{1g} modes associated with the MBT and BT layers, respectively (Fig. 2f)[18]. These frequencies are hardly changed in the superlattice family (MBT)$(\text{BT})_n$ for $n \geq 1$, reflecting the fact that the 1.2-THz and 1.8-THz modes are intrinsic to the individual MBT and BT layers. Moreover, as the electronic structures of (MBT)(BT) near the Brillouin zone centre are mainly contributed by the p_z orbitals, the c-axis A_{1g} modes lead to the strongest modulation of the orbital overlaps and thus the electronic binding energies. Fitted with cosine functions, the coherent responses to the 1.8-THz and 1.2-THz modes exhibit initial phases close to integer multiples of π (Fig. 2c insets), manifesting the displacive excitation of coherent phonons (DECP)[19]. Notably, DECP leads to fully symmetric A_1 modes in the superlattice unit cell spanning one MBT layer and one BT layer[19]. This constrained symmetry is fully consistent with our mode assignments. Along the TSS dispersion, the existence and absence of the amplitude sign reversal for the MBT and BT A_{1g} modes, respectively, both agree with theoretical calculations (Supplementary Fig. 9). By performing a pixel-wise Fourier transform of the trARPES data, we obtain the FD-ARPES[14,16] maps at 1.8 THz and 1.2 THz (Fig. 2d,e). Notably, the oscillating TSS dispersion results in a pair of bands in FD-ARPES maps with opposite oscillation phases[20]. The momentum-independent and momentum-dependent phases along the TSS dispersion at 1.8 THz and 1.2 THz, respectively, corroborate well the EDC analysis in Fig. 2c. Finally, the 3.4-THz mode can be attributed to either a second MBT A_{1g} mode[18] or a putative surface symmetry-breaking BT mode[21]. This uncertainty precludes the use of the 3.4-THz mode to distinguish layer origins of electronic states.

Given the heterointerface of the (MBT)(BT) superlattice, there are extra phonon modes involving coordinated atomic movements from both the MBT and BT layers[18]. Among the extra phonon modes,

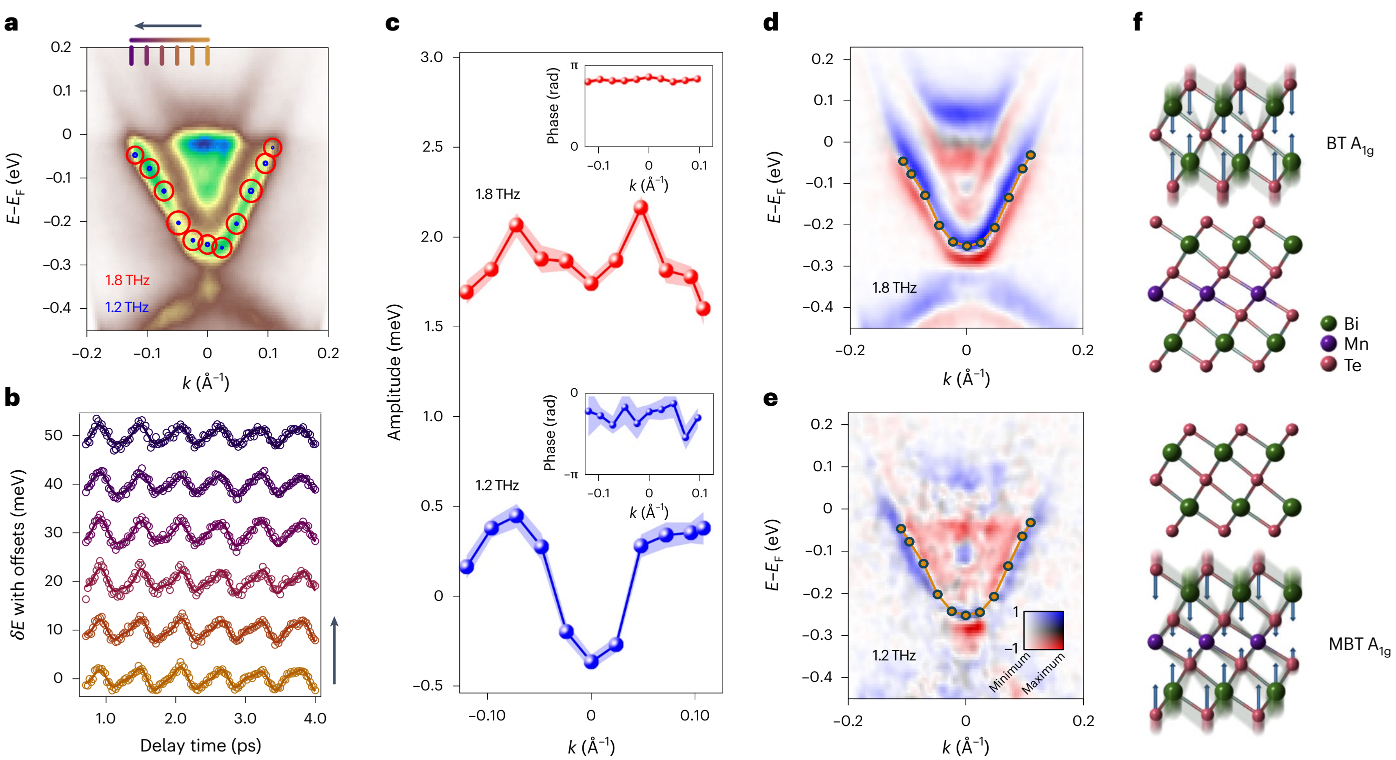

Fig. 2 | Coherent response of the TSS to phonon oscillations on the BT termination. **a**, Band dispersions cutting through $\bar{\Gamma} - \bar{K}$ taken at $t = 60$ fs. The sizes of the red and blue circles represent the oscillation amplitudes of the 1.8-THz and 1.2-THz modes, respectively. **b**, Oscillatory components of the TSS energy dynamics taken at different momentum k-points indicated by the gradient colour code in **a**. The oscillations are fitted to cosine functions. **c**, Oscillation amplitudes of the 1.2-THz and 1.8-THz modes, with the initial phases shown in the insets. Data are presented as mean values and the shaded widths indicate the error bars, which represent ± one-standard-deviation (1σ) uncertainties of the fitting results. **d**,**e**, Phase maps in FD-ARPES at the frequencies of the BT A_{1g} mode (1.8 THz) (**d**) and the MBT A_{1g} mode (1.2 THz) (**e**). The red–blue contrast indicates $\cos(\phi)$ where ϕ is the initial phase of the oscillation. The intensity saturation indicates the oscillation amplitude of FD-ARPES. In each FD-ARPES map, the intensities are normalized by the maximum value in the energy–momentum space. **f**, Cartoons of atomic vibrations corresponding to the BT and MBT A_{1g} modes.

we restricted our consideration to all the A_{1g} modes within the enlarged unit cell. This is based on the fact that the 1.5 eV optical excitation with a penetration depth of ~16.7 nm[22] is largely homogeneous for the top few unit cells, and hence the symmetry selection rules imposed by the DECP mechanism can allow only fully symmetric modes[19]. In the frequency range of interest, only the 1.2-THz MBT A_{1g} mode and the 1.8-THz BT A_{1g} mode were relevant to our observations, enabling us to use layer-specific phonon modes to probe the layer origins of electronic states. We also considered broken-symmetry modes at the material surface[21,23]. Yet, to the best of our knowledge, no such modes have been identified in (MBT)(BT) in the vicinity of 1.2 THz and 1.8 THz.

The dominant coupling between the TSS and the BT A_{1g} mode shows a strong localization of the TSS on the top BT layer. This result is fully consistent with theoretical expectations, and sets the foundation to tackle the more non-trivial case of the MBT termination.

We turn to the trARPES measurement on the MBT termination. The TSS and RS hybridize on this termination, resulting in a distinctively large electron-like pocket. This electron pocket has a stronger TSS character near $\bar{\Gamma}$, and a stronger RS character off $\bar{\Gamma}$ (Fig. 3b). We implemented the aforementioned EDC analysis on this hybridized electron pocket and extracted band energy dynamics. The obtained coherent oscillations suggested the existence of multiple frequency components (Fig. 3c). As evidenced by FFT (Supplementary Fig. 8b), two coherent modes exist at 1.8 THz and 1.2 THz, which are dominant near and away from $\bar{\Gamma}$, respectively. We fit the coherent energy oscillations with two-cosine functions, and extract the oscillation amplitudes at different momenta (Fig. 3d), which fully corroborate the FFT results.

We highlight the most substantial discovery on the MBT termination: the TSS and RS band characters are one-to-one mapped to the oscillation amplitudes of the BT and MBT A_{1g} modes, respectively. This is further demonstrated by the FD-ARPES data for the 1.2-THz and 1.8-THz modes on the hybridized electron-like band (Fig. 3e,f). We explain that this observation suggests a wavefunction relocation of the TSS from the top MBT layer to the buried BT layer.

We invoke the fundamental theory of deformation potentials. Under the quasi-static assumption, lattice strain S induces the energy shift $\delta\epsilon$ of a Bloch state at momentum k and band index n. The energy shift is expressed as[24]:

$$\begin{aligned}\delta\epsilon_{k,n} &= D_{\mu\nu}(k,n)\,S_{\mu\nu}\\ D_{\mu\nu}(k,n) &= \langle k,n|\delta V^{\mu\nu}(r)|k,n\rangle\end{aligned} \tag{1}$$

where $D_{\mu\nu}(k,n)$ is the deformation potential and $\delta V^{\mu\nu}(r)$ is the effective one-electron potential. Therefore, a suppressed $\delta\epsilon$ can be traced down to a vanishing $S_{\mu\nu}$ or $D_{\mu\nu}$. Notably, a vanishing $S_{\mu\nu}$ can occur for low-symmetry modes because of the short-lived driving force[25]. However, the coherent modes under consideration are fully symmetric A_{1g} modes, rendering the first scenario unlikely. Moreover, $D_{\mu\nu}$ can vanish when the overall parity of $k,n|\delta V^{\mu\nu}(r)|k,n$ is odd[26]. However, our DFT calculations have predicted a non-vanishing $D_{\mu\nu}$ for the TSS energy shift in response to the MBT A_{1g} mode, assuming the TSS is localized on the top MBT layer (Supplementary Fig. 10). The DFT calculations also demonstrate that other possible contributing factors such as

https://doi.org/10.1038/s41567-023-02008-4

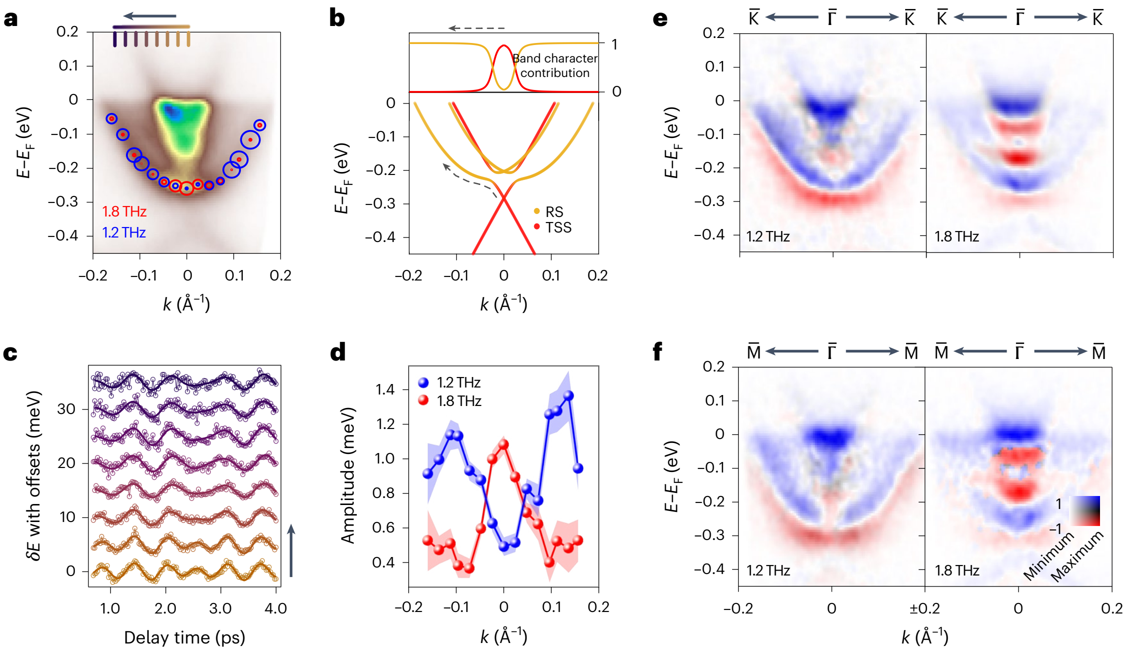

Fig. 3 | Coherent response on the MBT termination. a, trARPES spectra cutting through $\bar{\Gamma}-\bar{K}$ taken at $t = 60$ fs. The sizes of the red and blue circles represent the oscillation amplitudes of the 1.8-THz and 1.2-THz modes, respectively. **b**, Simulation of the RS–TSS hybridization using an effective Hamiltonian (Supplementary Note 1). The band characters on the modified RS are also plotted. **c**, Oscillatory components of the RS energy dynamics taken at different momentum k-points indicated by a gradient colour code in **a**. **d**, Oscillation amplitudes of the 1.2-THz and 1.8-THz modes, extracted by fitting coherent energy oscillations to two-cosine functions. Data are presented as mean values and the shaded widths indicate the error bars, which represent ± one-standard-deviation (1σ) uncertainties of the fitting results. **e**,**f**, FD-ARPES spectra of the 1.2-THz and 1.8-THz modes on the MBT termination along the $\bar{\Gamma}-\bar{K}$ direction (**e**) and along the $\bar{\Gamma}-\bar{M}$ direction (**f**). The red–blue contrast indicates $\cos(\phi)$ where ϕ is the initial phase of the oscillation. The intensity saturation indicates the oscillation amplitude of FD-ARPES. In each FD-ARPES map, the intensities are normalized by the maximum value in the energy–momentum space.

electronic screening[27] and kinematic constraints[28] do not play principal roles.

It is thus imperative to consider another scenario: the TSS wavefunction on the MBT termination is relocated into the BT layer (Fig. 4). The buried TSS will consequently exhibit a stronger coupling to the BT A_{1g} mode instead of the MBT A_{1g} mode, precisely reflecting our experimental observations. Microscopically, an increased van der Waals (vdW) gap between the top MBT layer and the second BT layer can push the TSS wavefunction into the deeper layers[13,29]. Our slab calculations demonstrate a substantial TSS relocation when the surface vdW gap exceeds the bulk counterpart by 10% (Supplementary Figs. 11 and 12), yet the increased vdW gap alone does not yield the RS. On the other hand, previous calculations incorporating Mn–Bi antisite defects yielded new band structures mimicking our observed RS[30]. Therefore, it is probably the combination of vdW gap increase and antisite defects that leads to the redistribution of the TSS wavefunction and the creation of the RS.

The layer origins of the TSS and RS shed light on the outstanding mystery of the near-gapless Dirac cones in antiferromagnetic (MBT)(BT)$_n$ superlattices[3–6,9–12]. An intense debate in the literature[3–12] centred around why the broken-symmetry gap on the MBT termination can vanish, despite the strong c-axis magnetic moments confirmed by magnetic force microscopy[31,32]. Our results indicate that the TSS on the MBT termination is partially pushed into the buried BT layer, and is less influenced by the surface magnetism. Such a wavefunction relocation has been discussed as a framework to reconcile experimental observations in ARPES[29] and scanning tunnelling microscopy[13] studies, yet this theoretical framework remains inconclusive because of the lack of a direct layer resolution, leaving alternative interpretations possible. For instance, although previous STS measurements[13] used this framework to explain the observed anomalous quasi-particle interference pattern, the alternative scenario using RS[11] challenged this interpretation. On the other hand, the experimentally evidenced wavefunction relocation in our work fully accounts for the near-gapless Dirac cone in (MBT)(BT) (Supplementary Fig. 12), and provides a hint to understand the phenomenology in pure MBT (Supplementary Note 4). Moreover, localization of the RS on the top MBT layer of (MBT)(BT) is directly shown for the first time, to our knowledge, explaining the energy gaps on the Rashba-like bands as observed in (MBT)(BT)$_n$ compounds[5,6,8,9]. To this end, our work resolves outstanding controversies[13,29,33] over the issue of broken-symmetry gaps in (MBT)(BT)$_n$ superlattices.

Our layer-encoded FD-ARPES experiment can be generalized to all magnetic topological superlattices (MBT)(BT)$_n$ and beyond. This approach will provide the foundational physics insight for how to engineer digital superlattices to manipulate topology and other collective quantum phenomena. Layer-encoded FD-ARPES requires the superlattice system to exhibit coherent phonon modes that are localized in individual layers. One needs to carefully examine the mode origins through the comparison with theory and with Raman spectroscopy. Symmetry-breaking modes can also exist on material surfaces or interfaces, which can provide further information on the origins of electronic states[21,23]. Our experiment manifests a profound measurement philosophy of 'seeing by listening,' whereby the frequency information from each layer allows us to visualize the layer origins of electronic states. This new philosophy is particularly important and timely, as emergent many-body physics such as superconductivity and non-trivial topology have been explored in stacked and twisted superlattices[34–38], yet little is known about their layer-by-layer wavefunction distribution using currently available spectroscopies. Our work potentially fills this technological gap. To this end, we believe that the impact of this experiment goes beyond resolving the long-standing

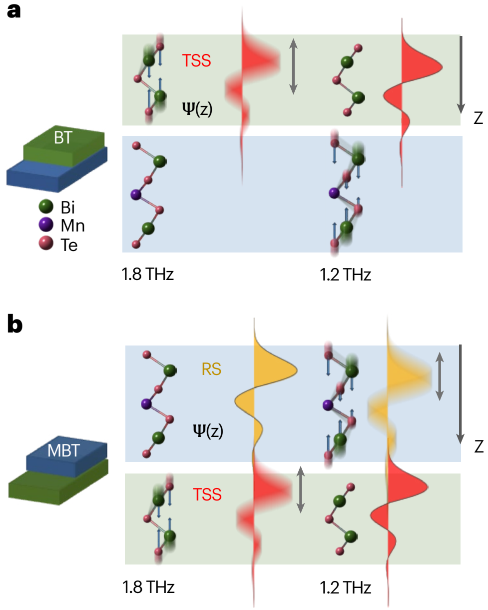

Fig. 4 | Schemes of layer-by-layer disentanglement of Bloch states. a,**b**, The BT and MBT A_{1g} phonon modes, as well as cartoons of the TSS and RS wavefunctions on the BT termination (**a**) and the MBT termination (**b**).

puzzles in MnBi$_{2n}$Te$_{3n+1,}$ and establishes a new paradigm for probing the spatial distribution of wavefunctions.

Online content

Any methods, additional references, Nature Portfolio reporting summaries, source data, extended data, supplementary information, acknowledgements, peer review information; details of author contributions and competing interests; and statements of data and code availability are available at https://doi.org/10.1038/s41567-023-02008-4.

References

1. Liu, C. et al. Robust axion insulator and Chern insulator phases in a two-dimensional antiferromagnetic topological insulator. *Nat. Mater.* **19**, 522–527 (2020).
2. Deng, Y. et al. Quantum anomalous Hall effect in intrinsic magnetic topological insulator MnBi$_2$Te$_4$. *Science* **367**, 895–900 (2020).
3. Klimovskikh, I. I. et al. Tunable 3D/2D magnetism in the (MnBi$_2$Te$_4$)(Bi$_2$Te$_3$)m topological insulators family. *npj Quantum Mater.* **5**, 54 (2020).
4. Hao, Y.-J. et al. Gapless surface Dirac cone in antiferromagnetic topological insulator MnBi$_2$Te$_4$. *Phys. Rev. X* **9**, 041038 (2019).
5. Chen, Y. J. et al. Topological electronic structure and its temperature evolution in antiferromagnetic topological insulator MnBi$_2$Te$_4$. *Phys. Rev. X* **9**, 041040 (2019).
6. Nevola, D. et al. Coexistence of surface ferromagnetism and a gapless topological state in MnBi$_2$Te$_4$. *Phys. Rev. Lett.* **125**, 117205 (2020).
7. Otrokov, M. M. et al. Prediction and observation of an antiferromagnetic topological insulator. *Nature* **576**, 416–422 (2019).
8. Shikin, A. M. et al. Sample-dependent Dirac-point gap in MnBi$_2$Te$_4$ and its response to applied surface charge: a combined photoemission and ab initio study. *Phys. Rev. B* **104**, 115168 (2021).
9. Li, H. et al. Dirac surface states in intrinsic magnetic topological insulators EuSn$_2$As$_2$ and MnBi$_{2n}$Te$_{3n+1}$. *Phys. Rev. X* **9**, 041039 (2019).
10. Vidal, R. C. et al. Orbital complexity in intrinsic magnetic topological insulators MnBi$_4$Te$_7$and MnBi$_6$Te$_{10}$. *Phys. Rev. Lett.* **126**, 176403 (2021).
11. Wu, X. et al. Distinct topological surface states on the two terminations of MnBi$_4$Te$_7$. *Phys. Rev. X* **10**, 031013 (2020).
12. Hu, C. et al. A van der Waals antiferromagnetic topological insulator with weak interlayer magnetic coupling. *Nat. Commun.* **11**, 97 (2020).
13. Yuan, Y. et al. Electronic states and magnetic response of MnBi$_2$Te$_4$ by scanning tunneling microscopy and spectroscopy. *Nano Lett.* **20**, 3271–3277 (2020).
14. Hein, P. et al. Mode-resolved reciprocal space mapping of electron–phonon interaction in the Weyl semimetal candidate *Td*-WTe$_2$. *Nat. Commun.* **11**, 2613 (2020).
15. Gerber, S. et al. Femtosecond electron–phonon lock-in by photoemission and X-ray free-electron laser. *Science* **357**, 71–75 (2017).
16. Suzuki, T. et al. Detecting electron–phonon coupling during photoinduced phase transition. *Phys. Rev. B* **103**, L121105 (2021).
17. Yan, C. et al. An integrated quantum material testbed with multi-resolution photoemission spectroscopy. *Rev. Sci. Instrum.* **92**, 113907 (2021).
18. Cho, Y. et al. Phonon modes and Raman signatures of MnBi$_{2n}$Te$_{3n+1}$ (n=1, 2, 3, 4) magnetic topological heterostructures. *Phys. Rev. Res.* **4**, 013108 (2022).
19. Zeiger, H. J. et al. Theory for displacive excitation of coherent phonons. *Phys. Rev. B* **45**, 768–778 (1992).
20. De Giovannini, U., Hübener, H., Sato, S. A. & Rubio, A. Direct measurement of electron–phonon coupling with time-resolved ARPES. *Phys. Rev. Lett.* **125**, 136401 (2020).
21. Shahil, K. M. F., Hossain, M. Z., Teweldebrhan, D. & Balandin, A. A. Crystal symmetry breaking in few-quintuple Bi$_2$Te$_3$ films: applications in nanometrology of topological insulators. *Appl. Phys. Lett.* **96**, 153103 (2010).
22. Jahangirli, Z. A. et al. Electronic structure and dielectric function of Mn–Bi–Te layered compounds. *J. Vac. Sci. Technol. B* **37**, 062910 (2019).
23. He, R. et al. Observation of infrared-active modes in Raman scattering from topological insulator nanoplates. *Nanotechnology* **23**, 455703 (2012).
24. Khan, F. S. & Allen, P. B. Deformation potentials and electron–phonon scattering: two new theorems. *Phys. Rev. B* **29**, 3341–3349 (1984).
25. Li, J. J., Chen, J., Reis, D. A., Fahy, S. & Merlin, R. Optical probing of ultrafast electronic decay in Bi and Sb with slow phonons. *Phys. Rev. Lett.* **110**, 047401 (2013).
26. Yang, S.-L. et al. Superconducting graphene sheets in CaC$_6$ enabled by phonon-mediated interband interactions. *Nat. Commun.* **5**, 3493 (2014).
27. Lee, W. S., Johnston, S., Devereaux, T. P. & Shen, Z.-X. Aspects of electron–phonon self-energy revealed from angle-resolved photoemission spectroscopy. *Phys. Rev. B* **75**, 195116 (2007).
28. Yang, S.-L. et al. Inequivalence of single-particle and population lifetimes in a cuprate superconductor. *Phys. Rev. Lett.* **114**, 247001 (2015).
29. Shikin, A. M. et al. Nature of the Dirac gap modulation and surface magnetic interaction in axion antiferromagnetic topological insulator MnBi$_2$Te$_4$. *Sci. Rep.* **10**, 13226 (2020).
30. Sitnicka, J. et al. Systemic consequences of disorder in magnetically self-organized topological MnBi$_2$Te$_4$ /(Bi$_2$Te$_3$)$_n$ superlattices. *2D Mater.* **9**, 015026 (2022).
31. Guo, J. et al. Coexisting ferromagnetic–antiferromagnetic phases and manipulation in a magnetic topological insulator MnBi$_4$Te$_7$. *J. Phys. Chem. C* **126**, 13884–13893 (2022).

32. Ge, W. et al. Direct visualization of surface spin-flip transition in $MnBi_4Te_7$. *Phys. Rev. Lett.* **129**, 107204 (2022).
33. Ma, X.-M. et al. Hybridization-induced gapped and gapless states on the surface of magnetic topological insulators. *Phys. Rev. B* **102**, 245136 (2020).
34. Geim, A. K. & Grigorieva, I. V. Van der Waals heterostructures. *Nature* **499**, 419–425 (2013).
35. Mak, K. F. & Shan, J. Semiconductor moiré materials. *Nat. Nanotechnol.* **17**, 686–695 (2022).
36. Island, J. O. et al. Spin–orbit-driven band inversion in bilayer graphene by the van der Waals proximity effect. *Nature* **571**, 85–89 (2019).
37. Kezilebieke, S. et al. Moiré-enabled topological superconductivity. *Nano Lett.* **22**, 328–333 (2022).
38. Can, O. et al. High-temperature topological superconductivity in twisted double-layer copper oxides. *Nat. Phys.* **17**, 519–524 (2021).

Publisher's note Springer Nature remains neutral with regard to jurisdictional claims in published maps and institutional affiliations.

Springer Nature or its licensor (e.g. a society or other partner) holds exclusive rights to this article under a publishing agreement with the author(s) or other rightsholder(s); author self-archiving of the accepted manuscript version of this article is solely governed by the terms of such publishing agreement and applicable law.

© The Author(s), under exclusive licence to Springer Nature Limited 2023

Methods

Sample growth

The $MnBi_4Te_7$ samples were synthesized using the melt growth method[39]. A high-purity Mn, Bi and Te mixture was sealed in carbon-coated quartz tubes under a high vacuum and heated in a muffle furnace at 900 °C for 5 hours, followed by a cool-down to 595 °C in 20 hours. The mixture was then slowly cooled down to 585 °C in 3 days (~0.14 °C h^{-1}) and annealed for 1 day. The single crystals were then obtained by water quenching at 585 °C. The samples were cleaved in situ under a base pressure lower than 8×10^{-11} mbar at 15 K.

ARPES measurements

All ARPES measurements were carried out at 15 K on the multi-resolution photoemission spectroscopy platform established at the University of Chicago[17]. Ultrahigh resolution μ-ARPES measurements were performed with a spatial resolution <10 μm and an energy resolution <4 meV using 205-nm probe pulses with an 80-MHz repetition rate. Ultrafast trARPES measurements were performed with an energy resolution of 17 meV and a time resolution of 115 fs at a 200-kHz repetition rate. Pump and probe wavelengths were 800 nm and 206 nm, respectively. The incident fluence was 350 μJ cm^{-2}. The integration of high-energy-resolution and high-time-resolution light sources in one set-up allowed us to combine complementary probes and obtain a holistic picture.

Computational details

All electronic structures were calculated with DFT as implemented in Vienna Ab initio Simulation Package[40,41]. The electron–electron interaction was mimicked with the projected augmented wave method[42] with the exchange-correlation interaction approximated by generalized gradient approximation (Perdew–Burke–Ernzerhof)[43]. A Hubbard U value of 5 eV was used for the d electrons of Mn. The energy cutoff for the plane-wave basis set was 350 eV. The surface states were calculated with a slab model of four [MBT + BT] layers (48 atoms in total), whereby the surfaces were fully relaxed under the experimental A-type antiferromagnetic configuration with the presence of DFT-D3 vdW correction[44]. A k-mesh of $9 \times 9 \times 1$ was used. The spin–orbit coupling was considered in all electronic structure calculations except for the surface relaxation.

Data availability

Source data are provided with this paper. All other data that support the plots and other findings of this study are available from the corresponding authors upon reasonable request.

References

39. Guan, Y. D. et al. Ferromagnetic $MnBi_4Te_7$ obtained with low-concentration Sb doping: a promising platform for exploring topological quantum states. *Phys. Rev. Mater.* **6**, 054203 (2022).
40. Kresse, G. & Furthmüller, J. Efficiency of ab-initio total energy calculations for metals and semiconductors using a plane-wave basis set. *Comput. Mater. Sci.* **6**, 15–50 (1996).
41. Kresse, G. & Furthmüller, J. Efficient iterative schemes for ab initio total-energy calculations using a plane-wave basis set. *Phys. Rev. B* **54**, 11169–11186 (1996).
42. Blöchl, P. E. Projector augmented-wave method. *Phys. Rev. B* **50**, 17953–17979 (1994).
43. Perdew, J. P., Burke, K. & Ernzerhof, M. Generalized gradient approximation made simple. *Phys. Rev. Lett.* **77**, 3865–3868 (1996).
44. Grimme, S., Antony, J., Ehrlich, S. & Krieg, H. A consistent and accurate ab initio parametrization of density functional dispersion correction (DFT-D) for the 94 elements H-Pu. *J. Chem. Phys.* **132**, 154104 (2010).

Acknowledgements

We acknowledge very helpful discussions with J. Sobota and P. Kirchmann from SLAC National Accelerator Laboratory, and with S. King, J. Park, P. Littlewood and S. Guha from the University of Chicago. The optimization of the static μ-ARPES set-up was partially supported by the US National Science Foundation (NSF) through grant no. DMR-2145373. The trARPES work was supported by the US Department of Energy (grant no. DE-SC0022960). The financial support for a part of sample preparation by S.H.L. was provided by the NSF through the Penn State 2D Crystal Consortium-Materials Innovation Platform (2DCC-MIP) under NSF cooperative agreement DMR-2039351. The sample synthesis efforts by Y.G. were supported by the US Department of Energy under grant DE-SC0019068. C.L. and R.M. acknowledge support from the Penn State MRSEC Center for Nanoscale Science through NSF grant no. DMR-2011839. B.Y. acknowledges financial support by the European Research Council under the European Union's Horizon 2020 research and innovation programme (grant no. 815869).

Author contributions

W.L., S.F.-M., C.Y. and S.Y. conducted the μ-ARPES and trARPES measurements. Y.G., S.H.L. and Z.M. grew the $(MnBi_2Te_4)(Bi_2Te_3)$ samples. H.T. and B.Y. performed first-principles calculations with input from R.M. and C.L. W.L., S.F.-M. and S.Y. wrote the manuscript with input from all co-authors. S.Y. conceived the experiment.

Competing interests

The authors declare no competing interests.

Additional information

Supplementary information The online version contains supplementary material available at https://doi.org/10.1038/s41567-023-02008-4.

Correspondence and requests for materials should be addressed to Shuolong Yang.

Peer review information *Nature Physics* thanks Rob Moore, Shunsuke Sato and the other, anonymous, reviewer(s) for their contribution to the peer review of this work.

Reprints and permissions information is available at www.nature.com/reprints.